ACS APPLIED NANO MATERIALS

High-Precision Assembly of Molecularly Thin Zeolite Nanosheets into Tiled Mono- and Multilayer Films for Robust Corrosion Protection

Ondřej Veselý, Nobuyuki Sakai,* Yasuo Ebina, and Takayoshi Sasaki

Cite This: *ACS Appl. Nano Mater.* 2026, 9, 6618−6630

Read Online

ACCESS | Metrics & More | Article Recommendations | Supporting Information

ABSTRACT: The fabrication of zeolite films by conventional hydrothermal methods limits their practical use because it produces irregular, nonuniform thick coatings under harsh synthesis conditions. In this study, to address these limitations, MCM-56 and bifer nanosheets exfoliated from their precursor layered zeolites were employed, and solution-based deposition methods were examined to prepare compact nanoscale-thick monolayer films of neatly tiled nanosheets under mild conditions. Atomic force microscopy revealed that spin coating, the pick-up method, and the Langmuir−Blodgett technique yielded high-quality monolayer films with predominantly monolayer coverage of >80% and low surface roughness (<1 nm), in contrast to the previously reported electrostatic adsorption method, which produced rough and uneven films. By repeating the deposition of monolayer films using the pick-up method, multilayer zeolite films were also successfully constructed. Their well-ordered stacked structure was confirmed by the progressive enhancement of the FT-IR band corresponding to Si−O−Si of the zeolite upon repeated deposition of monolayer films, as well as by the sharp X-ray diffraction peaks derived from the multilayer structure. The multilayer films were further deposited on a copper substrate, and their corrosion resistance was examined. As a result, the corrosion current density decreased by nearly an order of magnitude, and the corrosion potential shifted toward more positive values. These results indicate that highly ordered zeolite films exhibit pronounced anticorrosion effects while being deposited to a thickness of only tens of nanometers under mild conditions. These findings provide a general strategy for constructing highly ordered ultrathin zeolite films and expand the potential of zeolite nanosheets for functional surface coatings.

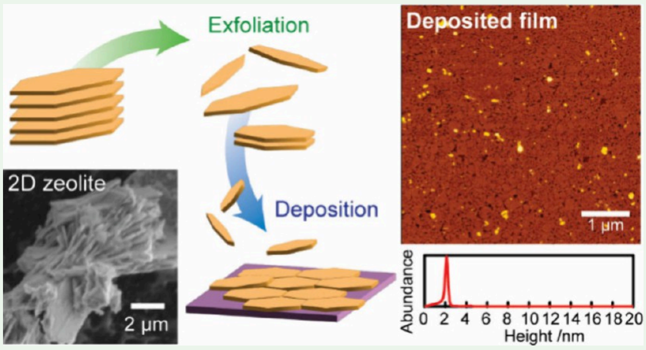

KEYWORDS: *zeolite nanosheets, layered materials, exfoliation, layer-by-layer deposition, spin-coating, Langmuir−Blodgett deposition, nanofilm deposition, anticorrosion*

■ INTRODUCTION

Two-dimensional (2D) nanosheets derived from layered inorganic materials have become valuable building blocks for constructing functional films and novel materials with controlled architectures.[1−5] Among these materials, zeolite nanosheets—exfoliated from layered precursors such as MCM-56 (MWW) and bifer (FER)[6−9]—remain relatively overlooked despite offering an interesting combination of the unique porosity, chemical and thermal stability and catalytic activity of zeolites while being processable as ultrathin 2D layers. Zeolites are crystalline microporous silicates and aluminosilicates (generally, with pores less than 1 nm in size) whose robust frameworks, adsorption, ion-exchange and catalytic properties, and stability under wide range of conditions have enabled widespread applications in catalysis and separation technologies.[10−13]

Although most known zeolite structures are three-dimensional,[14] a small subset of 2D zeolite precursors consists of discrete layers that can be delaminated into nanosheets with thicknesses of only a few nanometers or even just one or two unit cells.[15,16] Their layered nature offers a unique flexibility and variability in their applications; it not only enhances access to their active sites but also enables various textural modifications such as swelling or pillaring,[16−20] or transformation of the crystalline structure into a different zeolite framework using the layers as building blocks.[21−24] Notably, exfoliation of 2D zeolites into suspension of isolated nanosheets has also been a subject of extensive research.

Received: January 13, 2026
Revised: March 22, 2026
Accepted: March 27, 2026
Published: April 7, 2026

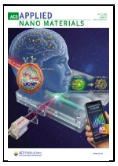

https://doi.org/10.1021/acsanm.6c00178

Early attempts at zeolite exfoliation utilized swelling by surfactants or shearing in melt; however, these methods were notably difficult and provided only limited yields.[7,25] Conversely, the soft chemical exfoliation emerged as a more promising method for the exfoliation of 2D zeolites into the suspension, allowing complete separation of layers under mild conditions and in high yields.[7,9,26] These suspensions can subsequently be utilized in the construction of composite materials and other structured forms, such as oriented disks and membranes, opening new possibilities for advanced material design.[8,9,26]

Aside from 2D zeolites, various exfoliated 2D materials, such as graphene, clays, metals, metal oxides, and MXenes, have demonstrated significant potential for advanced material design, especially in film fabrication or construction of nanoscale devices including capacitors, electrodes, and sensors.[27−31] These materials, when suspended in solution, enable layer-by-layer assembly using methods such as electrostatic adsorption,[32] the Langmuir−Blodgett (LB) method,[33] spin-coating,[34,35] drop casting,[36] and the pick-up method.[37] Among these, electrostatic adsorption is relatively facile and scalable but typically results in rough, irregular films with overlapping nanosheets.[32,38−40] Spin-coating under optimized conditions, by contrast, enables improved control over film thickness and uniformity by adjusting the concentration of the nanosheet suspension and rotation speed.[34,35,41] The pick-up method uses Marangoni convection to neatly assemble nanosheets into a monolayer film at the water−air interface. In principle, the method is similar to the LB technique; however, the nanosheet assembly is driven by forces at the phase interface instead of moving barriers, making it feasible to carry out without specialized equipment.[37,42,43] Similarly, the LB technique creates closely packed nanosheet layers transferable to solid substrates.[33] The method provides higher control over the deposition conditions, enabling more precise nanosheet arrangement on flat substrates as demonstrated on large variety of 2D materials.[5,31,34,37]

As one of various applications of nanosheet arrangement, a previous study has successfully demonstrated the use of titania nanosheet film as corrosion protection coating.[44] Zeolite-based films could offer several potential advantages. Their insulating nature, in contrast to the semiconducting character of titanium oxide, can further suppress electrochemical current flow between the metal substrate and the surrounding electrolyte. Moreover, the intrinsic pore system of zeolites can provide the capacity to host corrosion inhibitors or other active agents for self-healing.[45−47] Zeolite coatings have already been reported to effectively reduce corrosion of various metals, such as steel and aluminum alloys.[48,49] However, the reported zeolite films are typically around 10 μm thick, rough, and grown directly on substrates under harsh hydrothermal conditions, which may damage the coated materials. Consequently, although the protective capability of zeolite coatings has been demonstrated, relationship with the film thickness, control over its uniformity and structural ordering, and deposition under mild conditions remain unresolved. Previous work explored fabrication of zeolite nanosheet films via electrostatic adsorption.[38] However, films produced by this method generally exhibited rough surfaces and lacked higher-order structural regularity in nanosheet stacking. Therefore, it is possible that the intrinsic properties of zeolites have not been fully exploited. To take full advantage of the unique characteristics of zeolites, techniques capable of producing dense and well-organized packing of zeolite nanosheets are required.

In this study, to address the issue mentioned above, we employ zeolite nanosheets obtained via soft chemical exfoliation to demonstrate their applicability in fabricating uniform films only several nanometers thick. We make a comprehensive comparison of several key methods for the deposition of exfoliated zeolite nanosheets, including spin-coating, pick-up deposition, and LB method, all of which yield more compact and uniform films than the electrostatic adsorption. We further demonstrate that the pick-up method can rapidly produce highly ordered multilayer films under mild conditions, resulting in thin coatings (∼20 nm) that provide adequate corrosion protection of metal substrates despite their minimal thickness.

■ EXPERIMENTAL SECTION

Synthesis of MCM-56

The MCM-56 was prepared following an established procedure.[19] First, 2.0 g of 50% NaOH (Merck) was diluted with 52.8 mL of ultrapure water (Milli-Q, >18 MΩ cm) and subsequently 1.3 g of $NaAlO_2$ (≥53% Al_2O_3, Carl Roth) was dissolved in the mixture. Upon complete dissolution, 10.28 g of SiO_2 (Ultrasil VN3) was added, followed by 6.18 mL of hexamethylenimine (>98.0%, TCI). The mixture was transferred to a Teflon-lined steel autoclave and heated at 143 °C under rotation at 30 rpm for 32 h. The solid product was recovered by filtration, washed with ultrapure water, and dried at 60 °C.

Synthesis of Bifer

The bifer was synthesized following a previously published procedure.[9] The synthesis gel was prepared by mixing 30 mL of ultrapure water with 2.5 mL of 50% NaOH (Merck), 0.25 g of $NaAlO_2$ (≥53% Al_2O_3, Carl Roth), 10 g of choline chloride (>98.0%, Merck), and 16.2 g of 30% colloidal silica (prepared by diluting 12.15 g of LUDOX HS-40 (40%, Sigma-Aldrich) to the required concentration). The synthesis gel was stirred overnight at room temperature and subsequently transferred into a Teflon-lined steel autoclave. The crystallization was carried out at 150 °C with rotation at 30 rpm for 11 days. The solid product was recovered by centrifugation at 5000 rpm for 5 min, washed with water, and dried at 60 °C.

Exfoliation of MCM-56 and Bifer

The zeolite (MCM-56 or bifer) was dispersed in 10% aqueous solution of tetrabutylammonium (TBA) hydroxide (TBAOH, Fujifilm Wako) with the ratio of 60 mL g^{-1}. The mixture was shaken for 48 h at 180 rpm and subsequently centrifuged at 10,000 rpm for 30 min to separate the solid. The sediment was redispersed in the same volume of ultrapure water and shaken for another 48 h at 180 rpm. The obtained mixture was centrifuged to separate the suspension of exfoliated zeolite nanosheets from the unexfoliated solid for 30 min at 10,000 and 5000 rpm for the MCM-56 and bifer, respectively. The unexfoliated solid was redispersed in an equal volume of ultrapure water and the procedure was repeated one more time to obtain a second batch of the suspension.[38] The concentration of nanosheets in the suspension was estimated thermogravimetrically by heating an exact volume of the suspension in a platinum crucible at 85 °C to evaporate most of the solvent, followed by calcination at 450 °C for 6 h, and then measuring the weight of the remaining solid.

Substrate Preparation

Indium tin oxide (ITO) glass plates and Si wafers were used as substrates for the deposition. Prior to the deposition, the ITO glass plates were cut into the desired size (see each method separately) using a diamond-tip cutter and cleaned by oxygen plasma (PIB-20, Vacuum Device). The Si wafers were cleaned by immersion in a 1:1 methanol/HCl solution for 30 min and washed with copious amount

Scheme 1. Schematic of the Synthesis, Exfoliation, and Deposition of Zeolite Nanosheets

of ultrapure water. Subsequently, they were immersed in a concentrated H_2SO_4 for 30 min followed by thorough washing with ultrapure water.

Electrostatic Deposition

The cleaned substrate (5.0 cm × 1.0 cm) was immersed into a 20 g L^{-1} solution of polydiallyldimethylammonium chloride (PDDA, 20% in H_2O, Sigma-Aldrich, adjusted to pH 9 by addition of 2.5% TBAOH solution) for 15 min. The excess PDDA was washed away with copious amount of ultrapure water and subsequently the substrate was immersed for 15 min into a 0.08 g L^{-1} suspension of respective zeolite nanosheets adjusted to pH 9.1 with 0.01 M HCl, according to the conditions optimized in our previous work.[38] The coated substrate was washed with copious amount of ultrapure water and dried in air.[32]

Spin-Coating

Prior to the spin-coating, 1 mL of the aqueous suspension of zeolite nanosheets was centrifuged at 15,000 rpm for 30 min to sediment the nanosheets and decanted, and the sediment was redispersed in 0.5 mL dimethyl sulfoxide (DMSO, 99%, Fujifilm Wako) to obtain the zeolite nanosheets dispersed in DMSO.

ITO glass plates or Si wafers (1.5 cm × 1.5 cm) were used as substrates for the deposition. The cleaned substrate was anchored onto the sample holder of a Mikasa MS-B100 spin coater, covered with 60 μL of the DMSO-based suspension and rotated at the respective rotation speed for 800 s. The temperature was maintained at 26.5 ± 0.1 °C during the spin-coating.[35]

Pick-Up Deposition

The aqueous zeolite suspension was mixed with 99.5% ethanol in a 1:1 v/v ratio. A Petri-dish with an inner diameter of 93 mm was half-filled with ultrapure water and subsequently 8.62 μL of the prepared suspension was carefully dispensed onto the water−air phase boundary using a pipet to form a zeolite film on the liquid phase. The film was let to settle for 3 min (unless stated otherwise) before the deposition. The film was transferred onto the cleaned ITO glass plates or Si wafers (1.5 cm × 1.5 cm) by scooping it up from the phase boundary using tweezers with the substrate wafer itself. The coated substrate was placed onto a heater at 100 °C to evaporate the water.[37]

Langmuir−Blodgett (LB) Deposition

In a typical procedure, the zeolite nanosheet suspension was diluted with ultrapure water to a concentration of 8 mg L^{-1}, and was placed in the LB trough (USI FSD-3−777 double barrier Langmuir trough with Teflon coating, trough volume 250 mL, Wilhelmy-type balance for surface pressure measurement) at a regulated temperature of 25.0 ± 0.5 °C. After 30 min of equilibration, the barrier began compressing the suspension surface at a rate of 0.5 mm s^{-1} until the surface pressure reached 10 mN m^{-1}. The constant pressure was maintained for 30 min, and then the film at the interface was transferred onto the cleaned substrate (5.0 cm × 1.0 cm) by lifting up the preimmersed substrate at a rate of 1.0 mm min^{-1}.[33]

Anticorrosion Tests

Potentiodynamic polarization/Tafel curves and electrochemical impedance spectroscopy (EIS) data were obtained using a Solartron SI 1280B electrochemical measurement unit. The measurement was carried out in an aqueous 3.5 wt % NaCl solution with standard three-electrode system, where a zeolite-coated copper plate, a coiled Pt wire, and an Ag/AgCl (3 M NaCl) electrode served as the working electrode, the counter electrode, and the reference electrode, respectively. Polished copper plates were separately coated with 3, 5, or 10 subsequent layers of bifer nanosheets using the pick-up method, and with 10 layers using the electrostatic adsorption. The coated copper plates were covered with a Kapton tape with circular 5.5 mm hole, topped with an O-ring and placed into a Teflon-made evaluating cell (Plate Material Evaluating Cell, BAS Inc.). The measurements were performed on the sample polarized at ± 150 mV with respect to its open circuit potential (OCP) at a scan rate of 0.167 mV s^{-1} after the systems reached their steady-state condition (stable OCP) for at least 60 min. Values of corrosion potential and corrosion current density were determined from the intersection of linear fits to the measured anodic and cathodic current. The EIS data were acquired at OCP with an amplitude of 5 mV and a frequency range from 10 kHz to 100 mHz.

Characterization

X-ray diffraction (XRD) data were collected using a Rigaku Ultima IV powder diffractometer with monochromatized Cu Kα radiation (λ = 0.15406 nm). Scanning electron microscopy (SEM) images were obtained using a JEOL JSM-6010LA SEM at an acceleration voltage of 1 and 3 kV for deposited nanosheets and bulk samples, respectively. In-plane XRD measurements were performed using synchrotron X-ray radiation (λ = 0.11988(4) nm) at BL-6C, Photon Factory, High Energy Accelerator Research Organization (KEK). AFM imaging was carried out using a Hitachi AFM5200S scanning probe microscope equipped with a SI-DF20 cantilever in tapping mode. Zeta potential of the nanosheet suspensions was analyzed using an Otsuka Electronics ζ-potential and particle size analyzer ELSZ-2. Brewster angle microscopy (BAM) images were collected using the Kibron G-BAM equipped with a 660 nm excitation laser, set at an incident angle of 53° (the Brewster angle for the air/water interface) relative to the surface normal. Fourier-transform infrared (FT-IR) spectra were recorded using the Thermo Scientific Nicolet Summit X FT-IR spectrometer equipped with iD1 Transmission module. The peak areas were obtained by integration of the area under the peak between 980 and 1150 cm^{-1}. Cross-sectional transmission electron microscopy (TEM) images of the 10-layer bifer nanosheet films deposited on Si wafers were obtained using a JEOL JEM-2100F1 field-emission transmission electron microscope (FE-TEM) operated at an acceleration voltage of 200 kV. The TEM specimen was prepared by a focused ion beam (FIB) process after depositing carbon on the film. The adhesion test was performed by applying and removing an adhesive tape in accordance with the ISO 2409 standard on the 10-layer bifer film.

Simulation of XRD Profiles

Simulation of basal diffraction patterns has been conducted based on the bifer structure according to the previously reported procedure. The layer structure factor F was calculated according to the eq 1:[9,32,33]

$$F = \sum_j n_j f_j \exp\left(2\pi i\left(2z_j\frac{\sin\theta}{\lambda}\right)\right) \quad (1)$$

where n_j, f_j, θ, and λ are the number of atoms, atomic scattering factors, diffraction angles, and X-ray wavelength, respectively. The intensity I was estimated as the product of Laue interference function and the square of the structure factor as described in the eq 2:

Table 1. Characteristics of the Deposited Zeolite Films Depending on the Deposition Methods Derived from AFM Measurements[a]

method	zeolite	Ra (nm)	uncovered (%)	monolayer (%)	overlaps (%)
electrostatic adsorption	MCM-56	3.04 ± 0.48	19.8	38.3	41.9[b]
	bifer	2.25 ± 0.12	19.3	33.3	47.4[b]
spin-coating	MCM-56	1.02 ± 0.10	13.1	67.5	19.4
	bifer	0.48 ± 0.08	4.5	90.8	4.7
pick-up	MCM-56	1.04 ± 0.19	4.9	79.3	15.8
	bifer	0.66 ± 0.07	3.3	85.1	11.6
Langmuir–Blodgett	MCM-56	0.74 ± 0.03	<1	89.6	10.4
	bifer	0.75 ± 0.04	8.0	74.9	17.1

[a] Three 5 μm × 5 μm images each. [b] It includes not only double layers but also overlaps of three or more layers.

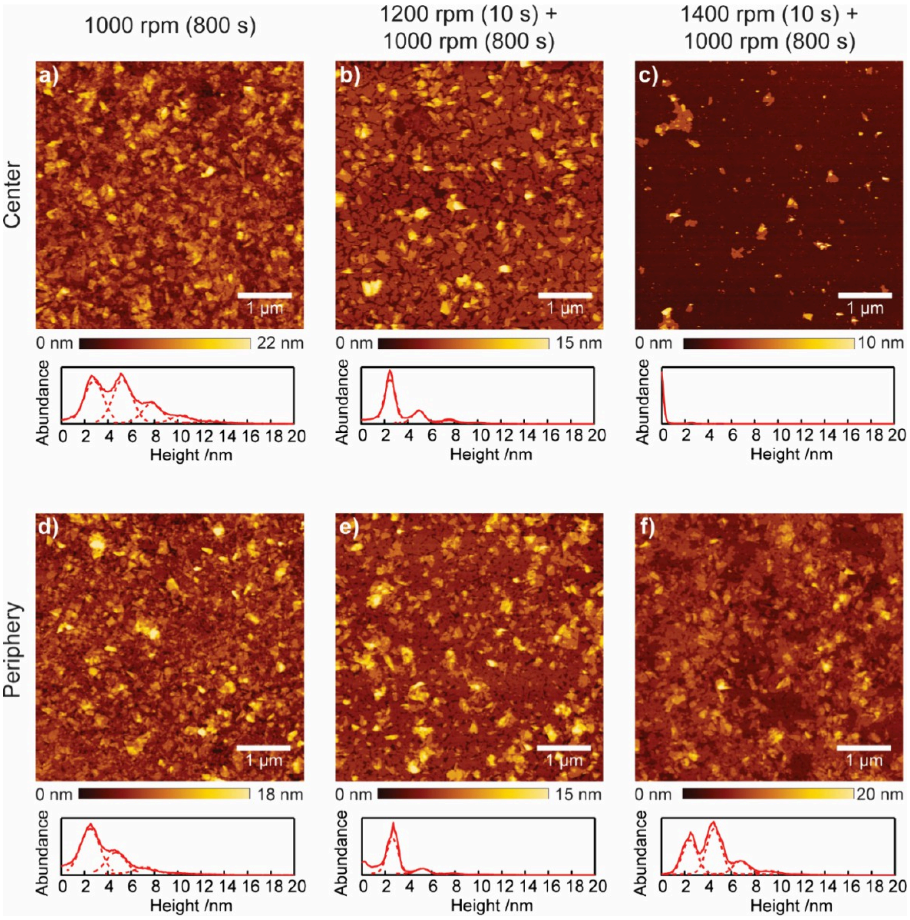

Figure 1. AFM images and corresponding height histograms of MCM-56 nanosheets deposited on the Si wafer by spin-coating their suspension (0.4 wt % in DMSO) at (a, d) 1000 rpm, (b, e) 1200 rpm followed by 1000 rpm, and (c, f) 1400 rpm followed by 1000 rpm.

$$I = F \cdot F^{*} \cdot \frac{\sin^2(\pi N h)}{\sin^2(\pi h)} \tag{2}$$

where the second term is the Laue interference function and $N = 10$ in this case.

■ RESULTS AND DISCUSSION

Exfoliated Nanosheets and Their Assembly via Electrostatic Adsorption

Layered zeolites MCM-56 and bifer were synthesized and exfoliated by following previously established procedures (Scheme 1),[8,38] yielding colloidal suspensions of single-layer nanosheets with lateral dimensions ranging from 0.2 to 0.5 μm and thickness ca. 2.5 nm for MCM-56 and 2.1 nm for bifer (Figures S1 and S2), which are in good agreement with previously reported dimensions of single-layer nanosheets, supporting successful exfoliation to single-layer sheets. The preservation of their intrinsic crystalline structure was confirmed by in-plane XRD measurements (Figure S3). The observed diffraction peaks matched the intralayer reflections reported for MCM-56 and bifer, consistent with both theoretical patterns and prior literature, verifying the preservation of their internal structure after exfoliation.

The previous work investigated the electrostatic adsorption and optimized the deposition conditions. Coating with 0.08 g L^{-1} for 15 min provided coverage between 80% and 90% both for MCM-56 and bifer nanosheets. We repeated the experiments, verifying the previous results and using the data for

https://doi.org/10.1021/acsanm.6c00178
ACS Appl. Nano Mater. 2026, 9, 6618−6630

comparison purposes.[32,38,39] While this method is facile and straightforward, it consistently produced films with significant nanosheet overlap and high roughness due to the rather irregular adsorption of nanosheets to the substrate surface (Figure S4). The average surface roughness (Ra) and ratios of area which is uncovered, covered by monolayer, and covered by overlapping nanosheets of the prepared films are summarized in Table 1. These are consistent with previously reported data.[38]

Spin-Coating of Zeolite Nanosheets

Previous studies have successfully used spin-coating to achieve dense packing of titania nanosheets.[5,35] Therefore, we examined the possibility of using this method to produce compact films of zeolite nanosheets. Spin-coating was applied to a 0.4 wt % suspension of MCM-56 nanosheets in DMSO to demonstrate the applicability of the method to the zeolite nanosheets in forming a highly uniform film. At 1200 rpm, uncovered dark areas at the substrate center were evident in the SEM images (Figure S5a−c), but these diminished with decreasing speed to 1100 rpm (Figure S5d−f), and disappeared entirely at 1000 rpm (Figure S5g−i), which resulted in a complete substrate coverage. However, AFM images revealed significant nanosheet overlaps (Figure 1a, d), showing that 62% of the area at the center and 35% at the peripheral regions were covered by more than one layer (Scheme S1 illustrates how single-layer nanosheets, gaps, and overlaps appear in AFM images, as well as the definition of the center and peripheral regions of the substrate), suggesting the need for optimization of the spin-coating conditions. A two-step rotation process was devised and employed to minimize overlaps; with an initial high-speed step (1200−1400 rpm for 10 s) to expel the excess suspension from the substrate, followed by a prolonged low-speed rotation (1000 rpm for 800 s) to slow down solvent evaporation and providing sufficient time for the nanosheets to self-assemble on the solvent surface and to deposit a uniform monolayer film. At an initial speed of 1200 rpm followed by 1000 rpm, nearly perfect monolayer films were obtained, with 67% of the area at both the center and peripheral regions covered by a single layer, while minor overlaps accounted for up to 26% at the center and 12% at the peripheral regions (Figures 1b, e and Figure S6a−c). The surface roughness was estimated to be 1.03 nm, which is much smoother than that of the film obtained by the electrostatic adsorption process (Table 1). In contrast, initial speeds exceeding 1400 rpm caused film breakage, leaving large, uncovered areas and reducing surface coverage. While an AFM image obtained at the substrate center showed total coverage only 2%, an image obtained at the peripheral regions showed 64% of its area covered by overlapping nanosheets (Figure 1c, f and Figure S6d−f).

The same workflow applied to a 0.4 wt % suspension of bifer nanosheets in DMSO proved less complex. A single-step rotation at 1000 rpm resulted in complete substrate coverage (Figure S7a−c), though AFM images revealed significant nanosheet overlaps, with 40% of the area covered by a single layer and 48% by overlapping nanosheets (Figure 2a). Increasing the rotation speed to 1200 rpm produced a near-perfect monolayer with 96% surface coverage, showing only minor ruptures in the center and 5% overlapping nanosheets, while 91% of the area was covered by a single-layer (Figure 2b and Figure S7d−f). This eliminates the need for the two-step rotation used for MCM-56. The surface roughness was estimated to be 0.50 nm, which is even smaller than that of the MCM-56 film (Table 1). We successfully achieved a well-ordered monolayer tiling of zeolite nanosheets via the spin-coating method.

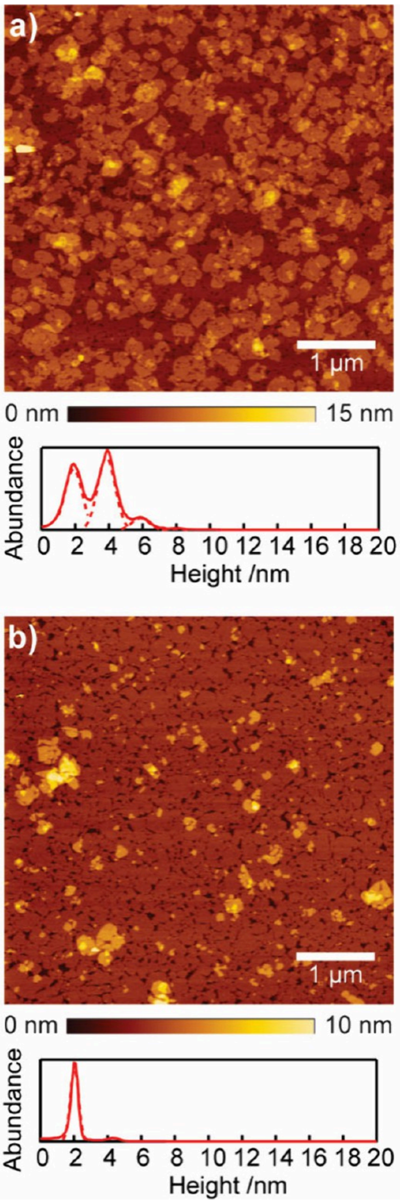

Figure 2. AFM images and corresponding height histograms of bifer nanosheets deposited on the Si wafer by spin-coating their suspension (0.4 wt % in DMSO) at (a) 1000 rpm and (b) 1200 rpm.

Assembly of Zeolite Nanosheets via Pick-Up Method

Subsequently, we applied the pick-up method to a 0.3 wt % suspension of MCM-56 nanosheets in a water/ethanol mixture, and the film forming at the water−air interface was scooped and transferred onto a Si substrate. Strikingly, the results varied depending on the timing of the transfer. When the film was picked up immediately after applying the suspension onto the water surface, it exhibited significant overlaps, and only 57% of the substrate was covered by a monolayer, as observed in the AFM image (Figure 3a). However, delaying transfer by 3 min resulted in a neatly tiled monolayer, covering 92% of the surface with only occasional overlaps up to 15% of the area (Figure 3b). The surface

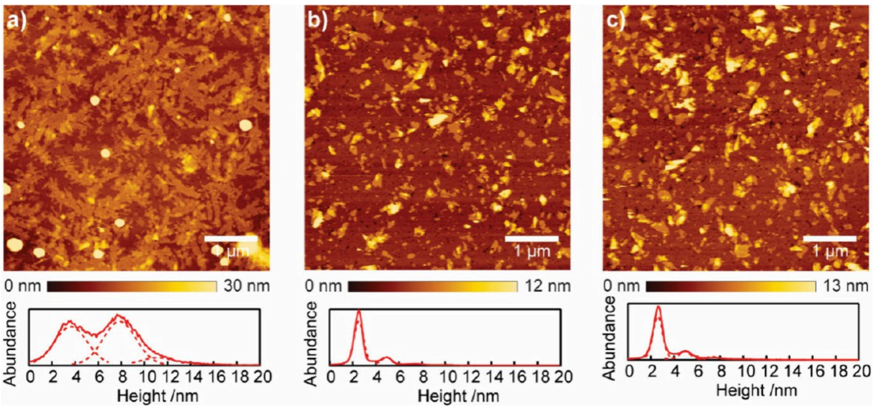

Figure 3. AFM images and corresponding height histograms of MCM-56 nanosheets deposited on the Si wafer from their suspension (0.3 wt % in 1:1 (w/w) water/ethanol mixture) by the pick-up method (a) without delay, (b) after 3 min delay, and (c) after 30 min delay.

roughness was estimated to be 0.91 nm, which is comparable to that of the film prepared by spin-coating (Table 1). BAM observations revealed that the film formed almost instantly at the water−air interface upon introducing the suspension, with no significant macroscopic changes occurring during the delay period (Figure S8). We speculated that the improved film uniformity after a delay is likely a result of larger multilayer aggregates submerging and sinking to the bottom. Nevertheless, extending the delay to 30 min yielded no further improvement with a certain small degree of overlapping nanosheets persisting (Figure 3c). It implies that the monolayer forms relatively quickly; however, a certain delay before deposition is required. Although 3 min cannot be regarded as a key parameter, a reproducible monolayer film was consistently obtained as long as a sufficient waiting time (3−30 min) was allowed.

Comparable results were observed for bifer nanosheets, with overlaps diminishing further at a reduced concentration of 0.25 wt %, yielding a neatly tiled film (Figure 4). This concentration adjustment, however, did not yield similar improvements for MCM-56 nanosheets. Overall, the method produced well-ordered monolayer films in a rapid and straightforward manner, and with high quality comparable to those obtained by spin-coating.

Deposition of Zeolite Nanosheet Films via Langmuir−Blodgett (LB) Method

Next, we focused on the deposition of zeolite nanosheets via the LB method which has demonstrated high precision in assembling various oxide nanosheets including $Ti_{0.87}O_2$.[33] LB deposition of MCM-56 nanosheets at a surface pressure of 10 mN m^{-1} with an MCM-56 suspension concentration of 8 mg L^{-1} (Figure S9a) resulted in a densely packed film, with 89% of the substrate covered by a single layer, as confirmed by AFM (Figure 5b), suggesting that the behavior of the MCM-56 nanosheets closely resembles that of the $Ti_{0.87}O_2$ nanosheets. The surface roughness was estimated to be 0.75 nm, which is comparable to that of the films prepared by spin-coating and pick-up methods (Table 1). However, occasional nanosheet overlaps accounting for up to 10% of the area were observed. Reducing the concentration to 4 mg L^{-1} in order to diminish the overlaps created significant gaps between nanosheets (26% of the area), compromising film integrity (Figure 5a). Conversely, increasing the concentration to 16 mg L^{-1} caused excessive overlaps (21% of the area), with some nanosheets aggregating into larger multilayer domains (Figure 5c).

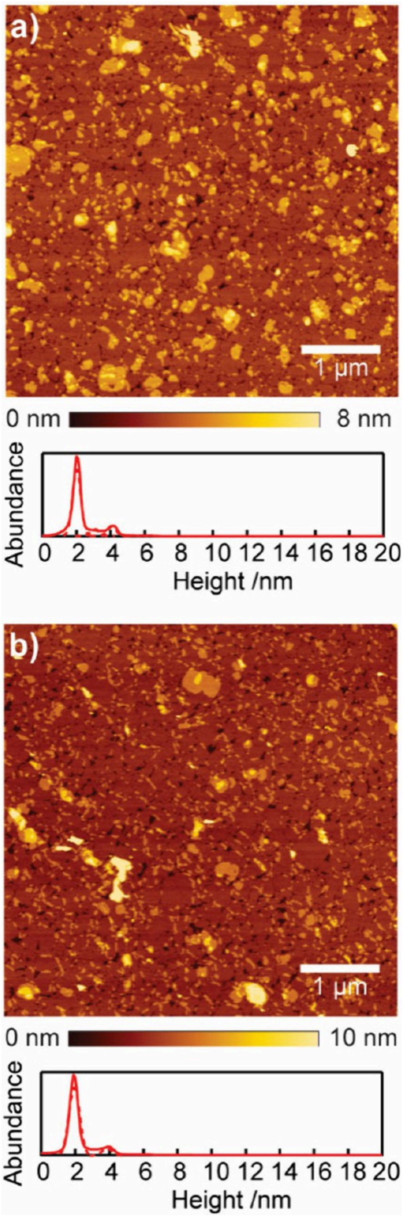

Figure 4. AFM images and corresponding height histograms of bifer nanosheets deposited on the Si wafer via the pick-up method from (a) 0.3 wt % and (b) 0.25 wt % suspensions.

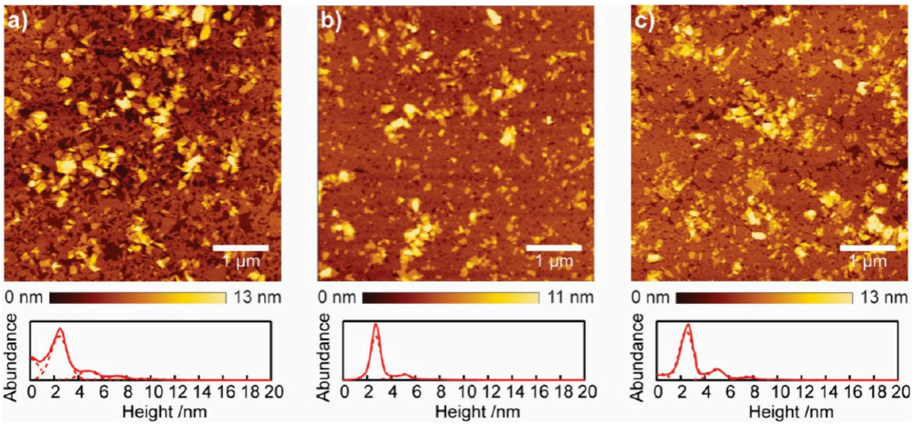

Figure 5. AFM images and corresponding height histograms of MCM-56 nanosheets deposited on the Si wafer by the LB method at a surface pressure of 10 mN m^{-1} with nanosheet concentrations of (a) 4 mg L^{-1}, (b) 8 mg L^{-1}, and (c) 16 mg L^{-1}.

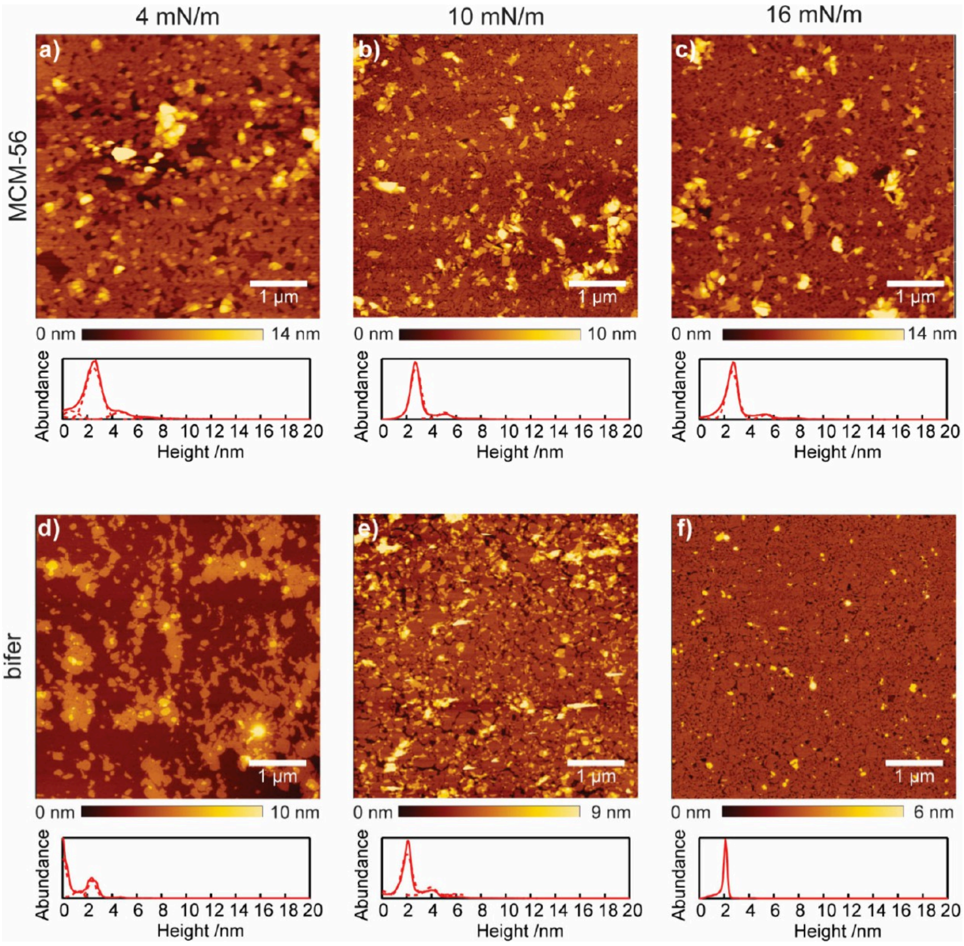

Figure 6. AFM images and corresponding height histograms of (a−c) MCM-56 and (d−f) bifer nanosheets deposited on the Si wafer by the LB method at a concentration of 8 mg L^{-1} and surface pressures indicated at the top.

The LB deposition of MCM-56 nanosheets as well as bifer nanosheets was also performed under various surface pressures (Figure S9b, c). Decreasing the surface pressure from 10 mN m^{-1} (Figure 6b, e) to 4 mN m^{-1} led to less dense nanosheet packing and the formation of gaps in the films for both MCM-56 and bifer (16% and 63% of the area, respectively), while some nanosheet overlaps persisted accounting for 11% of the area in both cases (Figure 6a, d). Remarkably, increasing the surface pressure to 16 mN m^{-1} led to a decrease in the number of overlaps to 10% and 1%, respectively, and to generation of new gaps between the nanosheets (7% and 3% of the area, respectively; Figure 6c, f), showing a deviation from the behavior previously observed for the $Ti_{0.87}O_2$ nanosheets where increasing the surface pressure only produces more overlaps.[33] This phenomenon was particularly apparent in the bifer film (Figure 6e, f); upon increasing the surface pressure from 10 to 16 mN m^{-1} virtually all overlaps between the nanosheets disappeared, accompanied by a decrease of typical

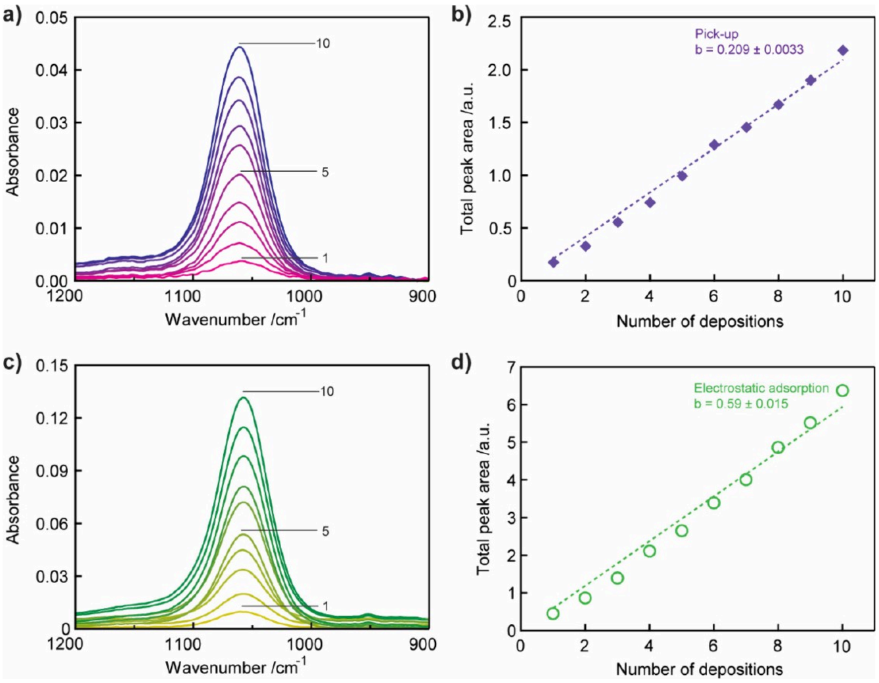

Figure 7. FT-IR spectra and the area of the peak at 1058 cm^{-1} plotted against the number of consecutive deposition cycles showing the build-up process of multilayer films of bifer nanosheets on the Si wafer using (a, b) the pick-up method and (c, d) the electrostatic adsorption.

nanosheet lateral size. This observation suggests that the increased pressure forces more nanosheets to overlap. The previous studies reported the tendency of oversized $Ti_{0.87}O_2$ nanosheets to submerge over time. The lateral dimensions of MCM-56 and bifer zeolite nanosheets, ranging from 0.2 to 0.5 μm, eliminate such concerns for single-layer nanosheets. However, the overlapping nanosheets may form larger multilayer particles with reduced buoyancy, which subsequently sink to the bottom of the trough. This produces temporary gaps in the film which are eventually filled by smaller nanosheets. The LB method also successfully yielded the well-ordered monolayer films of zeolite nanosheets.

Comparison of the Deposition Methods

The examined deposition methods each demonstrate unique advantages and limitations, that need to be taken into an account before their applications. The electrostatic adsorption is relatively straightforward, allows for automation, and can be scaled up efficiently, but owing to the nature of the principle, the resulting films are inherently disordered and rough (Figure S4), which does not meet the objective of achieving compact, uniform films. The films produced by the latter three methods (spin-coating, pick-up, and LB) are comparable in quality; compact and uniform, featuring occasional overlaps (Table 1) which appear to stem from nanosheet suspension properties, particularly the nanosheet aggregation dependent on ζ-potential and pH, rather than the deposition methods themselves (Figures S10, S11).

The spin-coating process offers high precision and versatility when optimized, producing compact and uniform films as confirmed by AFM imaging (Figures 1b, 2b, and Figure S12). However, it is highly sensitive to experimental conditions, such as temperature and humidity, and requires solvent exchange with DMSO, making it less favorable compared to water-based techniques.[35] Maintaining uniform coverage becomes increasingly challenging with larger substrates due to the need for tightly controlled deposition parameters, which limits its practical scalability and makes it most suitable for relatively small substrates (typically ~1.5 cm × 1.5 cm).

In contrast, the pick-up method stands out for its simplicity, time-efficiency, and minimal equipment requirements, producing high-quality uniform films (Figures 3b, 4b). Film formation occurs through self-assembly at the water−air interface, enabling deposition without specialized instrumentation while allowing transfer onto substrates of diverse size, shape, and composition, including Si and ITO glass. Previous studies by Osada et al. demonstrated that the process can be extended to printing or continuous roll-transfer approaches, indicating strong potential for large-area and industrial-scale fabrication. Although control over nanosheet packing during deposition is inherently less direct than in the other methods, the pick-up method produces films of comparable quality to spin-coating or LB method.

Finally, the LB method achieves uniform films with excellent nanosheet packing, as the internanosheet spacing can be tuned by adjusting the compression barriers (Figures 5b, 6e). This feature can yield high film uniformity, but the method requires specialized instrumentation, large volumes of nanosheet suspension, and significantly longer processing times. Moreover, the attainable coating area is constrained by the size of the LB trough. Among the studied techniques, the pick-up method emerges as the most practical choice, combining excellent film quality with operational simplicity, cost-effectiveness, and scalability—properties previously demonstrated for other materials,[37] but shown here for the first time to extend to zeolite nanosheets, opening a straightforward and scalable route to fabricate high-quality zeolite nanofilms.

Construction of Multilayer Films

To assess their suitability of these fabrication methods for practical applications, where multiple stacked layers may be required, we further explored repeated deposition into a multilayer film. The layer-by-layer buildup of the multilayer films by repeating the monolayer deposition of bifer nanosheets using the pick-up method was followed by FT-IR spectroscopy, which revealed a systematic increase in the intensity of the Si−O−Si asymmetric stretching vibration band at 1058 cm^{-1}.[38] The total peak area increased by approximately 0.209 ± 0.003 units per each deposition cycle (Figure 7a, b), reflecting the consistent growth of the multilayer film. In comparison, the multilayer build-up achieved via electrostatic adsorption exhibited a consistent increase of the 1058 cm^{-1} peak area by 0.590 ± 0.015 units per cycle (Figure 7c, d). The value was expected to be approximately two-times higher, as electrostatic adsorption inherently deposits nanosheets on both sides of the substrate, while the pick-up method coats only one. The net nanosheet uptake normalized per film was thus approximately 1.41 times higher for the electrostatic adsorption method, likely due to its disorderly deposition, where frequent overlaps result in a denser but less regular film. Deconvolution of the height histograms presented in Figure S4b and 4b reveals that the substrate is covered by 1.63 and 1.08 layers of nanosheets on average when coated using the electrostatic adsorption and pick-up method, respectively. Comparison of these values yields a ratio of 1.51, which is in close agreement with the step value ratio of 1.41 obtained from FT-IR spectroscopy. This agreement suggests that the densely packed film achieved in the first layer is successfully reproduced and accumulated through ten repeated depositions using the pick-up method.

To examine the stacking order of bifer nanosheets, XRD analysis was conducted on the multilayer films. For films deposited by electrostatic adsorption, the as-prepared sample exhibited a broad diffraction peak corresponding to an interlayer spacing of 2.49 nm (Figure 8a). Upon calcination, the peak became narrower and shifted to 1.79 nm, as a result of combustion of TBA ions and dehydration. The obtained value is slightly lower than the reported bifer nanosheet thickness of 1.87 nm, consistent with previously published data.[38] In contrast, films prepared by the pick-up method showed sharp, intense diffraction peaks already in the as-deposited state, indicating a high degree of nanosheet ordering (Figure 8b). The observed spacing of 2.23 nm is in excellent agreement with the predicted 2.22 nm, derived from the sum of the bifer nanosheet thickness (1.87 nm) and the intercalated TBA$^+$ layer (0.35 nm).[50,51] After calcination, the diffraction peak shifted to 1.83 nm, matching closely with the bifer nanosheet thickness. The experimental XRD patterns are in a good agreement with the simulated patterns, matching the peak positions as well as attenuation of the intensity of the first order reflection after calcination (Figure 8b, Figure S13). The superior ability of the pick-up method to produce well-ordered bifer nanosheet films is clearly demonstrated by the good agreement with the simulated data and sharper, higher intensity of the observed peaks compared to those from the films prepared by the electrostatic adsorption.

The improvement in the film organization is further supported by cross-sectional TEM imaging. Films prepared by electrostatic adsorption exhibit less ordered stacking of nanosheets, resulting in incomplete condensation and the formation of gaps between adjacent layers (Figure 9a). Consequently, the films display an average thickness of 31.2 ± 2.5 nm, corresponding to more than ten nominal layers. The disorderly stacking causes broadening of the XRD reflections indicative of reduced structural ordering. In contrast, films fabricated by the pick-up method show an assembly of densely packed nanosheets with a film thickness of 22.0 ± 2.3 nm, which is noticeably thinner than the film prepared by the electrostatic adsorption due to the absence of observable voids (Figure 9b). The high-resolution image (Figure 9c) shows a clear lamellar pattern suggesting a parallel alignment of the nanosheets with an elementary thickness of 2.1 ± 0.1 nm, consistent with the interlayer distance indicated by XRD. The total film thickness of 22.0 ± 2.3 nm corresponds to 10−12 stacked layers, consistent with AFM height analysis and FT-IR spectroscopic data.

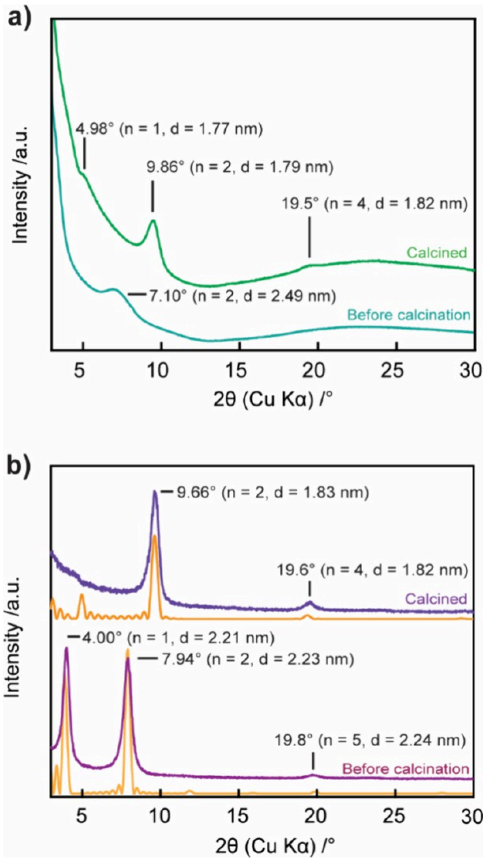

Figure 8. Simulated (orange) and experimental XRD patterns of bifer nanosheets deposited in 10 consecutive layers (a) by the electrostatic adsorption and (b) by the pick-up method.

Furthermore, in-plane XRD patterns were collected for the 10-layer bifer film prepared by the pick-up method (Figure S14). The patterns show sharp high-intensity diffraction peaks characteristic for the bifer material proving the film integrity both directly after deposition and after calcination.[38] The notable absence of *h*00 reflections further proves the parallel orientation of the nanosheets and highly ordered nature of the deposited film. The 10-layer film also exhibited sufficient adhesion to the substrate as demonstrated by a peeling test with adhesive tape. The AFM images and FT-IR spectra (Figure S15) collected prior to and after the test show only negligible difference, confirming the durability of the films.

Corrosion Protection Properties

To explore a practical application of the densely packed zeolite nanofilms, we evaluated their corrosion-protection performance. Mirror-polished copper plates with a surface roughness of 1.37 nm were coated with the as-prepared film of bifer nanosheets using the pick-up method under conditions described above. The resulting ten-layer film exhibited a significant reduction in corrosion current density, decreasing

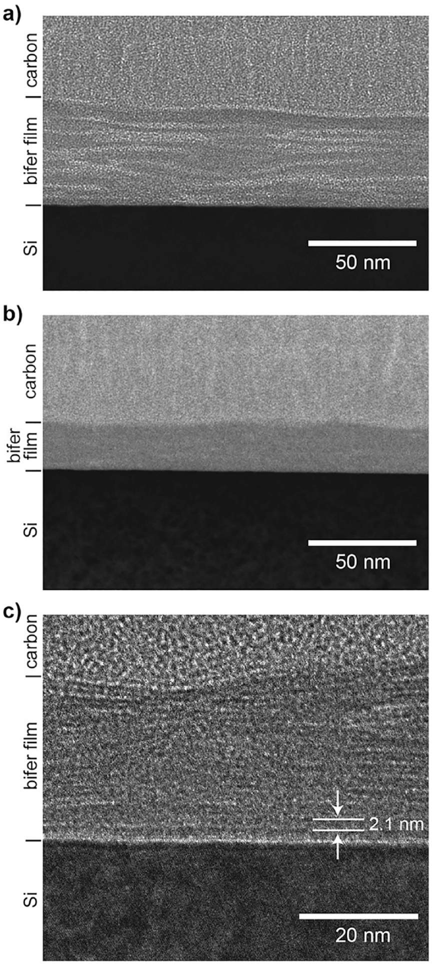

Figure 9. Cross-sectional TEM images of bifer nanosheets deposited using (a) the electrostatic adsorption and (b, c) pick-up method in 10 consecutive layers onto a Si substrate. TEM images reproduced with permission from Y. Nakayama and Y. Nemoto.

from 2.32 × 10^{-7} to 3.79 × 10^{-8} A cm^{-2}, accompanied by a positive shift in corrosion potential from −0.179 to −0.110 V (Figure 10a). These changes indicate a marked enhancement in corrosion resistance provided by the nanosheet coating. Systematic variation of the film thickness (3, 5, and 10 layers) revealed a gradual decrease in corrosion current density and a corresponding positive shift in corrosion potential (Figure 10b), confirming that the protective effect strengthens with increasing film thickness.

In comparison, as-prepared coating by 10 layers via the electrostatic adsorption also reduced the corrosion current but only to 2.21 × 10^{-7} A cm^{-2} and shifted the corrosion potential to −0.158 V (Figure S16), highlighting the superior corrosion inhibition properties of the compact, uniform film produced by the pick-up method. Compared with earlier studies that have demonstrated reductions of 2−7 orders of magnitude in corrosion current using 10 μm thick zeolite coatings grown under harsh hydrothermal or ionothermal conditions, which, while effective, can damage sensitive substrates,[48,49] our results show that a zeolite film only tens of nanometers thick can already suppress the corrosion current of copper by 1 order of magnitude while being deposited under mild and sensitive conditions.

Comparable corrosion protection has also been reported for other 2D nanosheet systems. Spray-coated $Ca_2Nb_3O_{10}$ films reduced the corrosion current by 3 orders of magnitude, although the coatings were substantially thicker (∼1 μm) and less structurally controlled requiring larger amounts of the material.[52] Similarly, $Ti_{0.87}O_2$ nanosheets assembled by electrostatic adsorption achieved significant protection, partly attributed to their larger lateral dimensions, which obstruct access to the coated surface more effectively.[44] Vapor-deposited boron nitride nanocoatings provided improvements comparable to those observed here but required more specialized processing.[53] These comparisons suggest that the lateral nanosheet size plays a decisive role, and that compact, well-organized assemblies can deliver adequate corrosion protection even at reduced thickness.

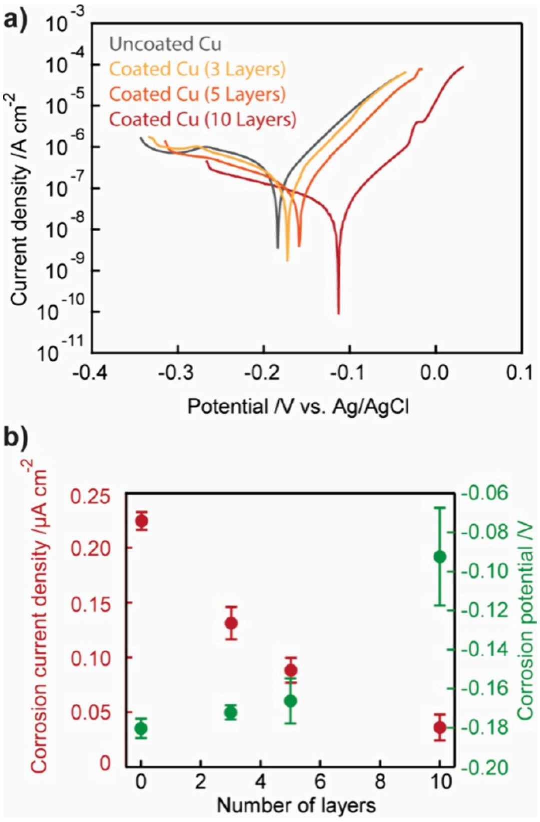

Figure 10. (a) Potentiodynamic polarization curves of the copper plates coated with 0, 3, 5, and 10 bifer layers and (b) corrosion current density and corrosion potential plotted as a function of number of bifer layers. The error bars were determined based on three measurements.

To gain a deeper understanding of the corrosion protection effect provided by the zeolite nanosheet coating, EIS measurements were conducted. Compared with the bare copper electrode, an increase in the charge transfer resistance was observed for the copper electrode coated with nanosheets (Figure S17). Furthermore, the charge transfer resistance increased monotonically with increasing number of nanosheet layers. These results suggest that the compact zeolite nanosheet coating physically inhibits contact between the copper surface and the electrolyte, thereby providing corrosion protection for the copper.

■ CONCLUSIONS

In the present work, we have examined the arrangement of exfoliated zeolite (MCM-56 and bifer) nanosheets into neatly tiled monolayer films by employing various deposition techniques. The deposition by electrostatic adsorption, while facile and experimentally undemanding, resulted in inherently less ordered and rough films. In contrast, the other deposition methods, such as spin-coating, pick-up, and LB method, produced uniform films of laterally aligned unilamellar nanosheets with only occasional overlaps. While yielding high-quality films, the spin-coating and LB methods were comparatively slower and equipment demanding. In contrast, the pick-up approach stood out for its simplicity, speed, and low equipment demands while yielding comparable film quality, making it a particularly effective and practical choice for fabricating high-quality zeolite thin films with low surface roughness. The method is also versatile with respect to the substrate, as nanosheet films can be assembled on various materials including Si, ITO, and copper, with previous studies demonstrating similar assembly on quartz glass and stainless steel. Furthermore, repeating deposition by the pick-up method produced well-ordered multilayer films of nanosheets. The zeolite nanofilms can effectively improve the corrosion resistance of copper by reducing the corrosion current and shifting the potential toward more positive values. The effect enhances more significant with increasing film thickness up to 10 consecutive layers, demonstrating significant corrosion suppression despite thickness of only several tens of nanometers, while being deposited under mild conditions in contrast to previous reports relying on micrometer-scale coatings grown under harsh conditions. These findings highlight the potential of zeolite nanosheet films as ultrathin, transparent, and chemically robust coatings for protective corrosion-resistant coatings which can be easily applied under mild conditions suitable even for sensitive materials.

■ ASSOCIATED CONTENT

Supporting Information

The Supporting Information is available free of charge at https://pubs.acs.org/doi/10.1021/acsanm.6c00178.

> Supplementary experimental details; Characterization of precursor layered materials and nanosheets; AFM images of zeolite nanosheet films prepared by electrostatic adsorption; SEM images of nanosheet films; BAM images of nanosheets assembled at the water−air interface; Pressure−area (π−A) isotherms during LB deposition; AFM images and height histograms of films prepared from nanosheet suspensions with various ζ-potentials; Structure factor calculated based on the bifer architecture; In-plane XRD patterns of 10-layer bifer nanosheet films; AFM images and FT-IR spectra before and after adhesion test; Potentiodynamic polarization curves of 10-layer bifer nanosheet film prepared by electrostatic adsorption; EIS data of bifer nanosheet film prepared by the pick-up method (PDF)

■ AUTHOR INFORMATION

Corresponding Author

Nobuyuki Sakai − *Research Center for Materials Nanoarchitectonics (MANA), National Institute for Materials Science (NIMS), Tsukuba, Ibaraki 305-0044, Japan;* orcid.org/0000-0002-9395-6751; Email: SAKAI.Nobuyuki@nims.go.jp

Authors

Ondřej Veselý − *Research Center for Materials Nanoarchitectonics (MANA), National Institute for Materials Science (NIMS), Tsukuba, Ibaraki 305-0044, Japan;* orcid.org/0000-0002-8350-7725

Yasuo Ebina − *Research Center for Materials Nanoarchitectonics (MANA), National Institute for Materials Science (NIMS), Tsukuba, Ibaraki 305-0044, Japan;* orcid.org/0000-0003-3471-9825

Takayoshi Sasaki − *Research Center for Materials Nanoarchitectonics (MANA), National Institute for Materials Science (NIMS), Tsukuba, Ibaraki 305-0044, Japan;* orcid.org/0000-0002-2872-0427

Complete contact information is available at: https://pubs.acs.org/10.1021/acsanm.6c00178

Notes

The authors declare no competing financial interest.

■ ACKNOWLEDGMENTS

This work was supported by World Premier International Research Center Initiative (WPI), Ministry of Education, Culture, Sports, Science and Technology (MEXT), Japan, and CREST of the Japan Science and Technology Agency (JST) (grant no. JPMJCR22B1), Japan. The in-plane XRD measurements were performed under the approval of the Photon Factory Program Advisory Committee (Proposal No. 2024G501). A part of this work was supported by "Advanced Research Infrastructure for Materials and Nanotechnology in Japan (ARIM)" of MEXT. Proposal Number JPMXP1225NM5077. We would like to thank Yoshiko Nakayama and Yoshihiro Nemoto (Electron Microscopy Unit, NIMS) for performing TEM observation and Yuki Hemmi (Materials Forming Unit, NIMS) for preparing of mirror-polished copper plates.

■ REFERENCES

(1) Schaak, R. E.; Mallouk, T. E. Perovskites by Design: A Toolbox of Solid-State Reactions. *Chem. Mater.* **2002**, *14*, 1455−1471.

(2) Lotsch, B. V. Vertical 2D Heterostructures. *Annu. Rev. Mater. Res.* **2015**, *45*, 85−109.

(3) Timmerman, M. A.; Xia, R.; Le, P. T. P.; Wang, Y.; ten Elshof, J. E. Metal Oxide Nanosheets as 2D Building Blocks for the Design of Novel Materials. *Chem.—Eur. J.* **2020**, *26*, 9084−9098.

(4) Jin, X.; Gu, T.-H.; Kwon, N. H.; Hwang, S.-J. Synergetic Advantages of Atomically Coupled 2D Inorganic and Graphene Nanosheets as Versatile Building Blocks for Diverse Functional Nanohybrids. *Adv. Mater.* **2021**, *33*, 2005922.

(5) Sakai, N.; Sasaki, T. Highly Organized Monolayer Arrangement of 2D Materials and Its Applications. *Acc. Mater. Res.* **2024**, *5*, 752−760.

(6) Roth, W. J.; Nachtigall, P.; Morris, R. E.; Čejka, J. Two-Dimensional Zeolites: Current Status and Perspectives. *Chem. Rev.* **2014**, *114*, 4807−4837.

(7) Roth, W. J.; Opanasenko, M.; Mazur, M.; Gil, B.; Čejka, J.; Sasaki, T. Current State and Perspectives of Exfoliated Zeolites. *Adv. Mater.* **2024**, *36*, 2307341.

(8) Roth, W. J.; Sasaki, T.; Wolski, K.; Song, Y.; Tang, D.-M.; Ebina, Y.; Ma, R.; Grzybek, J.; Kałahurska, K.; Gil, B.; Mazur, M.; Zapotoczny, S.; Cejka, J. Liquid Dispersions of Zeolite Monolayers with High Catalytic Activity Prepared by Soft-Chemical Exfoliation. *Sci. Adv.* **2020**, *6*, No. eaay8163.

(9) Roth, W. J.; Sasaki, T.; Wolski, K.; Ebina, Y.; Tang, D.-M.; Michiue, Y.; Sakai, N.; Ma, R.; Cretu, O.; Kikkawa, J.; Kimoto, K.;

Kalahurska, K.; Gil, B.; Mazur, M.; Zapotoczny, S.; Čejka, J.; Grzybek, J.; Kowalczyk, A. Exfoliated Ferrierite-Related Unilamellar Nanosheets in Solution and Their Use for Preparation of Mixed Zeolite Hierarchical Structures. *J. Am. Chem. Soc.* **2021**, *143*, 11052−11062.

(10) Serrano, D. P.; Centi, G.; Diddams, P. A.; Čejka, J. Outlooks for Zeolite Catalysts in a Low-Carbon Scenario. *Catal. Today* **2024**, *426*, 114365.

(11) Li, Y.; Li, L.; Yu, J. Applications of Zeolites in Sustainable Chemistry. *Chem* **2017**, *3*, 928−949.

(12) *Zeolites in Catalysis: Properties and Applications*; Čejka, J.; Morris, R. E.; Nachtigall, P., Eds.; Royal Society of Chemistry, 2017; Vol. *28*.

(13) Maesen, T. Chapter 1. The Zeolite Scene−An Overview. In *Studies in Surface Science and Catalysis*; Čejka, J., van Bekkum, H., Corma, A., Schüth, F., Eds.; Elsevier, 2007; Vol. *168*, pp 1−12.

(14) Baerlocher, C.; McCusker, L. B.; Brouwer, D.; Marler, B. *Database of Zeolite Structures*. https://www.iza-structure.org/databases/.

(15) Schreyeck, L.; Caullet, P.; Mougenel, J. C.; Guth, J. L.; Marler, B. PREFER: A New Layered (Alumino) Silicate Precursor of FER-Type Zeolite. *Micropor. Mater.* **1996**, *6*, 259−271.

(16) Roth, W. J.; Čejka, J.; Millini, R.; Montanari, E.; Gil, B.; Kubu, M. Swelling and Interlayer Chemistry of Layered MWW Zeolites MCM-22 and MCM-56 with High Al Content. *Chem. Mater.* **2015**, *27*, 4620−4629.

(17) Roth, W. J.; Kresge, C. T.; Vartuli, J. C.; Leonowicz, M. E.; Fung, A. S.; McCullen, S. B. MCM-36: The First Pillared Molecular Sieve with Zeolite Properties. In *Studies in Surface Science and Catalysis*; Beyer, H. K., Karge, H. G., Kiricsi, I., Nagy, J. B., Eds.; Elsevier, 1995; Vol. *94*, pp 301−308.

(18) Maheshwari, S.; Jordan, E.; Kumar, S.; Bates, F. S.; Penn, R. L.; Shantz, D. F.; Tsapatsis, M. Layer Structure Preservation during Swelling, Pillaring, and Exfoliation of a Zeolite Precursor. *J. Am. Chem. Soc.* **2008**, *130*, 1507−1516.

(19) Roth, W. J.; Chlubná, P.; Kubů, M.; Vitvarová, D. Swelling of MCM-56 and MCM-22P with a New Medium — Surfactant-Tetramethylammonium Hydroxide Mixtures. *Catal. Today* **2013**, *204*, 8−14.

(20) Roth, W. J.; Gil, B.; Mayoral, A.; Grzybek, J.; Korzeniowska, A.; Kubu, M.; Makowski, W.; Čejka, J.; Olejniczak, Z.; Mazur, M. Pillaring of Layered Zeolite Precursors with Ferrierite Topology Leading to Unusual Molecular Sieves on the Micro/Mesoporous Border. *Dalton Trans.* **2018**, *47*, 3029−3037.

(21) Opanasenko, M.; Shamzhy, M.; Wang, Y.; Yan, W.; Nachtigall, P.; Čejka, J. Synthesis and Post-Synthesis Transformation of Germanosilicate Zeolites. *Angew. Chem., Int. Ed.* **2020**, *59*, 19380−19389.

(22) Roth, W. J.; Gil, B.; Makowski, W.; Sławek, A.; Grzybek, J.; Kubu, M.; Čejka, J. Interconversion of the CDO Layered Precursor ZSM-55 between FER and CDO Frameworks by Controlled Deswelling and Reassembly. *Chem. Mater.* **2016**, *28*, 3616−3619.

(23) Eliášová, P.; Opanasenko, M.; Wheatley, P. S.; Shamzhy, M.; Mazur, M.; Nachtigall, P.; Roth, W. J.; Morris, R. E.; Čejka, J. The ADOR Mechanism for the Synthesis of New Zeolites. *Chem. Soc. Rev.* **2015**, *44*, 7177−7206.

(24) Díaz, U.; Corma, A. Layered Zeolitic Materials: An Approach to Designing Versatile Functional Solids. *Dalton Trans.* **2014**, *43*, 10292−10316.

(25) Sabnis, S.; Tanna, V. A.; Li, C.; Zhu, J.; Vattipalli, V.; Nonnenmann, S. S.; Sheng, G.; Lai, Z.; Winter, H. H.; Fan, W. Exfoliation of Two-Dimensional Zeolites in Liquid Polybutadienes. *Chem. Commun.* **2017**, *53*, 7011−7014.

(26) Roth, W. J.; Sasaki, T.; Wolski, K.; Gil, B.; Zapotoczny, S.; Čejka, J.; Kubů, M.; Mazur, M.; Ebina, Y.; Sakai, N.; Tang, D.-M.; Ma, R. Exfoliating Layered Zeolite MFI into Unilamellar Nanosheets in Solution as Precursors for the Synthesis of Hierarchical Nanocomposites and Oriented Films. *Inorg. Chem. Front.* **2023**, *10*, 1511−1521.

(27) Lim, K. R. G.; Shekhirev, M.; Wyatt, B. C.; Anasori, B.; Gogotsi, Y.; Seh, Z. W. Fundamentals of MXene Synthesis. *Nat. Synth.* **2022**, *1*, 601−614.

(28) Nicolosi, V.; Chhowalla, M.; Kanatzidis, M. G.; Strano, M. S.; Coleman, J. N. Liquid Exfoliation of Layered Materials. *Science* **2013**, *340*, 1226419.

(29) Stöter, M.; Rosenfeldt, S.; Breu, J. Tunable Exfoliation of Synthetic Clays. *Annu. Rev. Mater. Res.* **2015**, *45*, 129−151.

(30) Ma, R.; Sasaki, T. Nanosheets of Oxides and Hydroxides: Ultimate 2D Charge-Bearing Functional Crystallites. *Adv. Mater.* **2010**, *22* (45), 5082−5104.

(31) Hamasalih, G. H.; Ghaderi, S.; Hassanzadeh, A.; Hallaj, R.; Aziz, S. B. Enhanced Langmuir-Blodgett Deposition of Monolayer Gold Nanoplates for Multi-Modal Mercury Ion Detection. *Mater. Chem. Phys.* **2026**, *347*, 131505.

(32) Sasaki, T.; Ebina, Y.; Tanaka, T.; Harada, M.; Watanabe, M.; Decher, G. Layer-by-Layer Assembly of Titania Nanosheet/Polycation Composite Films. *Chem. Mater.* **2001**, *13*, 4661−4667.

(33) Akatsuka, K.; Haga, M.; Ebina, Y.; Osada, M.; Fukuda, K.; Sasaki, T. Construction of Highly Ordered Lamellar Nanostructures through Langmuir-Blodgett Deposition of Molecularly Thin Titania Nanosheets Tens of Micrometers Wide and Their Excellent Dielectric Properties. *ACS Nano* **2009**, *3*, 1097−1106.

(34) Matsuba, K.; Wang, C.; Saruwatari, K.; Uesusuki, Y.; Akatsuka, K.; Osada, M.; Ebina, Y.; Ma, R.; Sasaki, T. Neat Monolayer Tiling of Molecularly Thin Two-Dimensional Materials in 1 min. *Sci. Adv.* **2017**, *3*, e1700414.

(35) Sakai, N.; Sasaki, T. Guidelines for Arranging 2D Nanosheets into Neatly Tiled Monolayer Films by a Spin-Coating Process. *Langmuir* **2022**, *38*, 12399−12407.

(36) Shi, Y.; Osada, M.; Ebina, Y.; Sasaki, T. Single Droplet Assembly for Two-Dimensional Nanosheet Tiling. *ACS Nano* **2020**, *14*, 15216−15226.

(37) Shi, Y.; Li, H.; Tsunematsu, H.; Ozeki, H.; Kano, K.; Yamamoto, E.; Kobayashi, M.; Abe, H.; Chen, C.-W.; Osada, M. Ultrafast 2D Nanosheet Assembly via Spontaneous Spreading Phenomenon. *Small* **2024**, *20*, 2403915.

(38) Wang, C.; Sakai, N.; Ebina, Y.; Kikuchi, T.; Grzybek, J.; Roth, W. J.; Gil, B.; Ma, R.; Sasaki, T. Construction of Hierarchical Films via Layer-by-Layer Assembly of Exfoliated Unilamellar Zeolite Nanosheets. *Small* **2024**, *20*, 2308293.

(39) Polatoglu, I.; Cakicioglu-Ozkan, F. Aqueous Interactions of Zeolitic Material in Acidic and Basic Solutions. *Microporous Mesoporous Mater.* **2010**, *132*, 219−225.

(40) Decher, G. Fuzzy Nanoassemblies: Toward Layered Polymeric Multicomposites. *Science* **1997**, *277*, 1232−1237.

(41) Kim, J. W.; Kang, D.; Kim, T. H.; Lee, S. G.; Byun, N.; Lee, D. W.; Seo, B. H.; Ruoff, R. S.; Shin, H. S. Mosaic-like Monolayer of Graphene Oxide Sheets Decorated with Tetrabutylammonium Ions. *ACS Nano* **2013**, *7*, 8082−8088.

(42) Askounis, A.; Kita, Y.; Kohno, M.; Takata, Y.; Koutsos, V.; Sefiane, K. Influence of Local Heating on Marangoni Flows and Evaporation Kinetics of Pure Water Drops. *Langmuir* **2017**, *33*, 5666−5674.

(43) Lin, X.; Fang, G.; Liu, Y.; He, Y.; Wang, L.; Dong, B. Marangoni Effect-Driven Transfer and Compression at Three-Phase Interfaces for Highly Reproducible Nanoparticle Monolayers. *J. Phys. Chem. Lett.* **2020**, *11*, 3573−3581.

(44) Nurdiwijayanto, L.; Nishijima, H.; Miyake, Y.; Sakai, N.; Osada, M.; Sasaki, T.; Taniguchi, T. Solution-Processed Two-Dimensional Metal Oxide Anticorrosion Nanocoating. *Nano Lett.* **2021**, *21*, 7044−7049.

(45) Suzuki, M.; Hayashi, T.; Hikino, T.; Kishi, M.; Matsuno, T.; Wada, H.; Kuroda, K.; Shimojima, A. Integrated Extrinsic and Intrinsic Self-Healing of Polysiloxane Materials by Cleavable Molecular Cages Encapsulating Fluoride Ions. *Adv. Sci.* **2023**, *10*, 2303655.

(46) Xue, B.; Zong, X.; Wang, C.; Zhang, H.; Luo, J. Corrosion Inhibition of a Sol-Gel Coating Modified with Cobalt- Enriched

Zeolite on AA2024-T3 Aluminum Alloy. *Int. J. Electrochem. Sci.* **2019**, *14*, 10966−10982.

(47) Du, J.; Wang, Z.; Wei, Z.; Yao, J.; Song, H. An Environmental Friendly Self-Healing Coating with Silane/Ce-ZSM-5 Zeolite Structure for Corrosion Protection of Aluminum Alloy. *Surf. Coat. Technol.* **2022**, *436*, 128290.

(48) Beving, D. E.; McDonnell, A. M. P.; Yang, W.; Yan, Y. Corrosion Resistant High-Silica-Zeolite MFI Coating: One General Solution Formulation for Aluminum Alloy AA-2024-T3, AA-5052-H32, AA-6061-T4, and AA-7075-T6. *J. Electrochem. Soc.* **2006**, *153*, B325.

(49) Cai, R.; Sun, M.; Chen, Z.; Munoz, R.; O'Neill, C.; Beving, D. E.; Yan, Y. Ionothermal Synthesis of Oriented Zeolite AEL Films and Their Application as Corrosion-Resistant Coatings. *Angew. Chem., Int. Ed.* **2008**, *47*, 525−528.

(50) Veselý, O.; Eliášová, P.; Morris, R. E.; Čejka, J. Reverse ADOR: Reconstruction of UTL Zeolite from Layered IPC-1P. *Mater. Adv.* **2021**, *2*, 3862−3870.

(51) Lipkowski, J.; Komarov, V. Y.; Rodionova, T. V.; Dyadin, Y. A.; Aladko, L. S. The Structure of Tetrabutylammonium Bromide Hydrate $(C_4H_9)_4NBr\cdot2^1/_3H_2O$. *J. Supramol. Chem.* **2002**, *2*, 435−439.

(52) Yang, K.; Zhang, P.; Feng, Z.; Wang, Y.; Peng, J.; Li, B.-W. Solution-Processed Nanocoating of $Ca_2Nb_3O_{10}$ and Polydopamine for Anticorrosion on Magnesium Alloy. *Adv. Eng. Mater.* **2024**, *26*, 2400223.

(53) Duran, B.; Pat, S. Improved Corrosion Protection of Stainless Steel by Two Dimensional BN Nanomaterial Coating. *ECS J. Solid State Sci. Technol.* **2022**, *11*, 063017.